2016

Hydrothermal monitoring in Yellowstone National Park using airborne thermal infrared remote sensing

C. M.U. Neale
Utah State University, cneale@nebraska.edu

C. Jaworowski
Yellowstone Center For Resources, cjawo@vcn.com

H. Heasler
Yellowstone Center For Resources, heasler@vcn.com

S. Sivarajan
Utah State University, saravanan.sivarajan@ndsu.edu

A. Masih
Utah State University, masih.ashish@gmail.com

Remote Sensing of Environment 184 (2016) 628–644

Contents lists available at ScienceDirect

Remote Sensing of Environment

journal homepage: www.elsevier.com/locate/rse

Hydrothermal monitoring in Yellowstone National Park using airborne thermal infrared remote sensing

C.M.U. Neale [a,1], C. Jaworowski [b,2], H. Heasler [b,2], S. Sivarajan [a,3], A. Masih [a]

[a] Remote Sensing Services Laboratory, Civil and Environmental Engineering Dept., Utah State University, Logan, UT 84322, USA
[b] Yellowstone Center For Resources, Yellowstone National Park, WY 82190, USA

ARTICLE INFO

Article history:
Received 11 March 2014
Received in revised form 16 April 2016
Accepted 27 April 2016
Available online 1 August 2016

Keywords:
Airborne thermal infrared remote sensing
Hydrothermal systems
Emissivity
Yellowstone National Park

ABSTRACT

This paper describes the image acquisition and processing methodology, including surface emissivity and atmospheric corrections, for generating surface temperatures of two active hydrothermal systems in Yellowstone National Park. Airborne thermal infrared (8–12 μm) images were obtained annually from 2007 to 2012 using a FLIR SC640 thermal infrared camera system. Thermal infrared image acquisitions occurred under clear-sky conditions after sunset to meet the objective of providing high-spatial resolution, georectified imagery for hydrothermal monitoring. Comparisons of corrected radiative temperature maps with measured ground and water kinetic temperatures at flight times provided an assessment of temperature accuracy. A repeatable, time-sequence of images for Hot Spring Basin (2007–2012) and Norris Geyser Basin (2008–2012) documented fracture-related changes in temperature and fluid flow for both hydrothermal systems, highlighting the utility of methods for synoptic monitoring of Yellowstone National Park's hydrothermal systems.

1. Introduction

Established in 1872, Yellowstone National Park is famous for its globally rare collection of hydrothermal features - geysers, mud pots, steam vents, and hot springs. An unusual heat source, cold groundwater recharge, and a natural network of fluid flow pathways are necessary for these composite natural resources - hydrothermal features and the hydrothermal system. The U.S. Congress requires the monitoring of Yellowstone's hydrothermal system. Protection of Yellowstone National Park's hydrothermal systems involves the utilization of scientific information and knowledge about the geologic processes responsible for their occurrence.

Beginning in 2007, an airborne thermal infrared (TIR) monitoring technique was used to gather night baseline data for hydrothermal systems within Yellowstone National Park (YNP) using a FLIR SC640, broad-band (8–12 μm) TIR camera flown at 1800 m above ground level. Airborne image acquisition occurred during night and yielded uncorrected temperature images with 1-m spatial resolution. Fall and spring acquisitions minimized solar heating effects. Fall acquisitions also minimized the ground cooling effect of melting snow. Calibration and corrections for atmospheric effects in the imagery as well as emissivity of the ground resulted in temperature maps of the hydrothermal systems. Comparing derived radiative temperatures with ground temperatures of hydrothermal pools provided an assessment of the monitoring technique's thermal accuracy for various temperatures.

Remote sensing techniques have proven to be an effective means to monitor the Park's hydrothermal systems. These techniques complement geochemical monitoring, (Friedman, 2007), helicopter condition assessments of hydrothermal areas, and field studies. The goal of airborne acquisition was night TIR imagery with 1-m spatial resolution and 1 °C temperature accuracy. A 1-m spatial resolution permitted the detection of spatial change in a 1-m pool or area of ground. High-spatial resolution also enabled the detection and monitoring of hydrothermal changes within a short time frame such as 1-year or less. A 1 °C temperature accuracy will enable future radiative heat flow calculations with the desired accuracy. Airborne TIR remote sensing fills a niche between ground or helicopter reconnaissance and satellite-based remote sensing. Although TIR satellite imagery (Landsat, ASTER and MODIS) covers large areas effectively, the spatial resolution is too coarse (60 to 1000 m per pixel) for the detailed monitoring of changing hydrothermal systems.

Satellite-based remote sensing in the TIR part of the spectrum has been used to estimate surface energy balance components and evapotranspiration over large agricultural areas (Bastiaansen, Menenti, Feddes, & Holtslag, 1998; Kustas & Norman, 1999; Li, Kustas, Prueger, Neale, & Jackson, 2005; Taghvaeian & Neale, 2011) and monitor urban areas (Roberts, Quattrochi, Hulley, Hook, & Green, 2012). Satellite studies in YNP have (1) modeled snow-free areas using Landsat (Watson,

E-mail addresses: cneale@nebraska.edu (C.M.U. Neale), cjawo@vcn.com (C. Jaworowski), heasler@vcn.com (H. Heasler), saravanan.sivarajan@ndsu.edu (S. Sivarajan), masih.ashish@gmail.com (A. Masih).
[1] Presently at Daugherty Water for Food Institute, University of Nebraska, 2201 Transformation Drive, Suite 3220, Lincoln, NE 68,588, USA.
[2] Presently Independent Geologist, P.O. Box 1238, Powell, WY 82435, USA.
[3] Presently at Agricultural and Biosystems Engineering, North Dakota State University, Fargo, ND 58108, USA.

http://dx.doi.org/10.1016/j.rse.2016.04.016
0034-4257/

Lockwood, Newman, Anderson, & Garrott, 2008), (2) used Landsat summer imagery for park-wide monitoring of geothermal areas (Savage et al., 2010) and (3) used night ASTER and MODIS imagery for monitoring geothermal activity as well as estimating park-wide radiant geothermal heat flow (Vaughan, Kezthelyi, Lowenstern, Jaworowski, & Heasler, 2012). A recent literature review (Li et al., 2013) highlighted the challenges in extracting land surface temperatures from satellite sensors. Previous airborne remote sensing applications involved assessing water temperatures in rivers and streams (Torgesen, Faux, Mcintosh, Poage, & Norton, 2001) and estimating surface parameters (Quatrtrochi & Luvall, 2003).

This paper describes a TIR methodology for acquiring and processing baseline imagery used for monitoring two hydrothermal systems in Yellowstone National Park: Hot Spring Basin (HSB) and Norris Geyser Basin (NGB) (Fig. 1). These two hydrothermal systems were chosen because there was a possibility of significant surface temperature changes during the multi-year period of this study. Significant changes in the ground surface temperature at HSB may be expected to occur over a

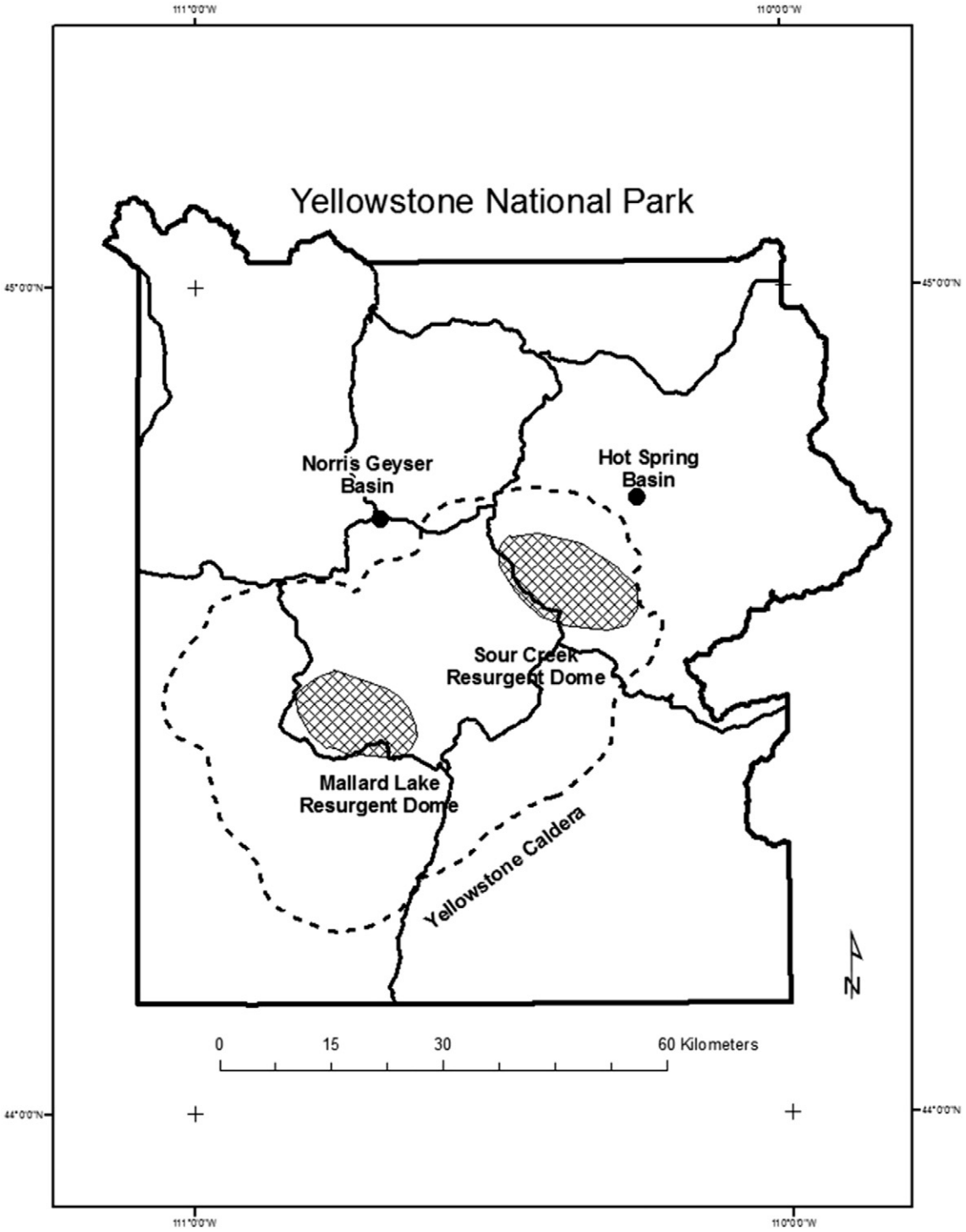

Fig. 1. Map showing location of NGB and HSB hydrothermal systems (black dots) within Yellowstone National Park. The map also highlights major roads (solid black lines), the 640,000 year-old Yellowstone caldera (black dashed line) and two resurgent domes (Mallard Lake and Sour Creek; cross-hatched areas). Geologic data from Christiansen (2001) and other digital information from NPS Data Store (http://www.nps.gov/gis/, accessed 17 September 2014).

Table 1
Calibrated image mosaics statistics for several flights over HSB and NGB. The maximum temperature is the maximum temperature on the night TIR mosaic.

Area	Date	Time (a.m.)	Maximum temperature	Air temperature	Air temperature source
HSB					
2007	9/13	12:06–12:19	50.74 °C	0.9 °C	NPS lake-WT
2008	9/12	11:52–12:13	67.56 °C	2.6 °C	NPS lake-WT
2009	9/10	1:17–1:37	69.37 °C	8.3 °C	NPS lake-WT
2010	9/25	11:45 p.m.–12:04	67.24 °C	6.6 °C	NPS lake-WT
2011	9/8	1:22–1:42	65.69 °C	6.9 °C	NPS lake-WT
2012	3/9	10:22–10:32 p.m.	63.00 °C	−2.6 °C	NPS lake-WT
0.5					
NGB					
2008	9/12	1:31–1:53	69.47 °C	−0.6 °C	Norris museum
2009	9/10	3:36–3:53	72.77 °C	2.5 °C	Norris museum
2010	9/25	12:33–12:49	75.11 °C	4.2 °C	Norris museum
2011	9/9	12:08–12:31	71.31 °C	5.8 °C	Norris museum
2012	3/9	9:23 p.m.	63.17 °C	−3.1 °C	Norris museum

short-time period because HSB has the shallowest depth to partially molten rock in YNP (Huang et al., 2015). Similarly, at NGB the dramatic changes in the behavior of hot springs and geysers noted by previous researchers (White, Hutchinson, & Keith, 1988) may be detected by high-spatial resolution airborne remote sensing. Thus, it is possible that significant changes in the ground surface temperature may occur over a short-time period and over a spatially extensive area at both HSB and NGB. Also, both hydrothermal systems contain acid-sulfate areas where a diffuse flow of hydrothermal fluids occurs over spatially extensive areas. Upflowing hydrothermal fluids over a large surface area, including heat, improved the possibility of detecting temperature changes. Therefore, the choice of HSB and NGB provided the best chance of testing a repeatable methodology for monitoring Yellowstone's hydrothermal systems and documenting each hydrothermal system's temperature variations and hydrothermal fluid flow.

2. Methods

The Utah State University (USU) airborne remote sensing system, image acquisition, and image processing for multispectral (MS) and TIR systems is the focus of the METHODS section of this paper. Discussion of the georectification and image processing procedures for day visible and night TIR images of these hydrothermal areas provides necessary information for the generated products. Image calibration, corrections for lens effects, mosaicking of individual images and atmospheric corrections of at-aircraft temperatures as well as emissivity corrections for soil, vegetation, earth and water generated corrected temperature mosaics used for assessing these hydrothermal systems.

2.1. Utah State University airborne remote sensing system

The USU airborne MS digital system used between 2007 and 2010 had three Kodak Megaplus 4.2i Digital Cameras with imaging sensors and producing images approximately 2000 × 2000 pixels (Cai & Neale, 1999). The Nikon 20 mm lenses had interference filters forming spectral bands centered in the green (0.55 μm), red (0.67 μm) and near-infrared (0.8 μm) portions of the electromagnetic spectrum. A porthole in the belly of a Cessna TU206 single engine aircraft) held the cameras within a high-grade aluminum/carbon composite mount. A FLIR SC640 camera with a 40 mm lens mounted through a different porthole and aligned with the MS system cameras acquired TIR imagery in the 8 to 12 μm range. Boards and software installed in a fast PC computer with two 500 GB hard drives for storage of the imagery controlled both the digital and TIR cameras. Since 2007, the USU airborne MS digital system and TIR imager (FLIR SC640) have been used in numerous applications that require high-spatial resolution imagery (Neale et al., 2012; Geli et al., 2012). In 2010, USU developed an integrated airborne MS system and LIDAR Assisted Stereo Imager (LASSI) LIght Detection and Ranging (LIDAR) system. The LIDAR system has a full-waveform Riegl Q560 LIDAR transceiver, and a Novatel SPAN *LN*-200 Global positioning system (GPS)/inertial measurement unit (IMU) Navigation System

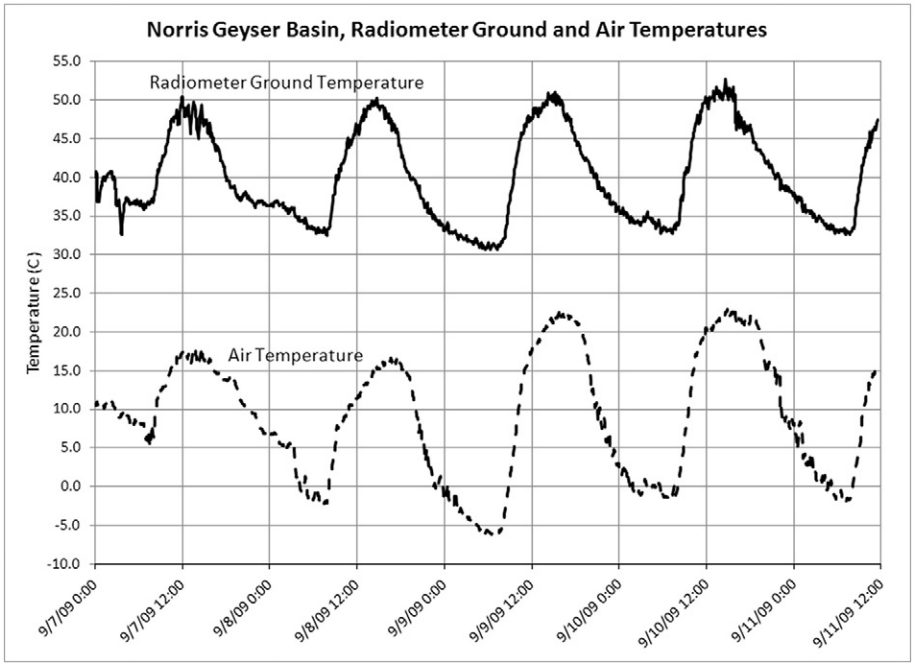

Fig. 2. Graph showing air and surface ground temperatures within NGB from September 7 through September 11, 2009. An infrared radiometer pointing to a hot, dry area labeled "Hydrothermal Explosion Crater" in Fig. 3 measured the surface ground temperatures.

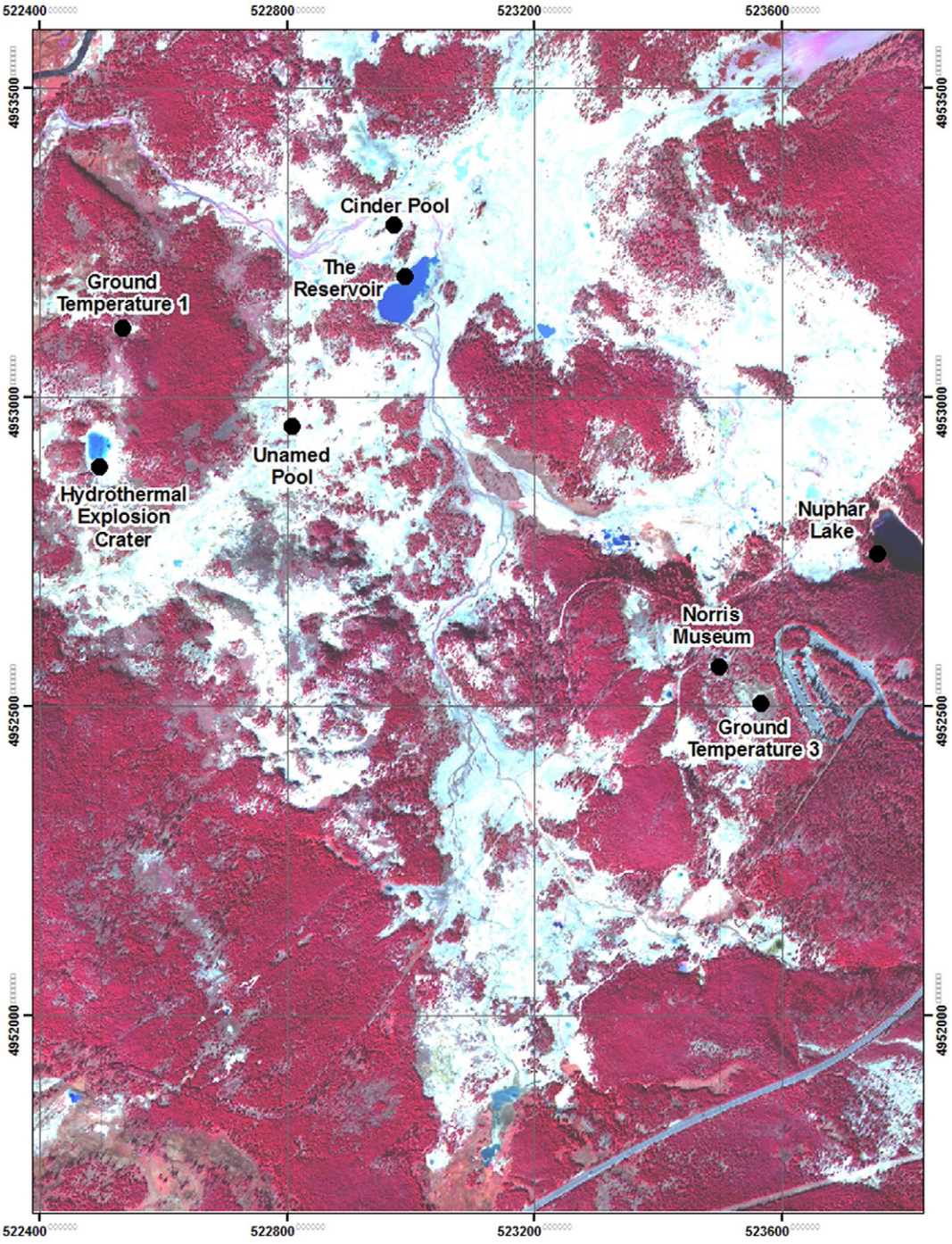

Fig. 3. Orthorectified visible image (MS-LIDAR) showing locations of kinetic temperature measurements in NGB. Imagery available at www.mbmg.mtech.edu/gis/gis-ArcGISservices.asp, accessed 28 September 2015.

(Neale, Pack, Sivarajan, and Masih, 2013). Rectified orthoimages were produced through direct georeferencing using the Terrascan and Terraphoto/Microstation software, data from the IMU system, LIDAR point cloud-based Triangular Irregular Networks (TINS), and the time stamped images.

2.2. Image acquisition

Image acquisitions for YNP occurred primarily during the month of September, a typically dry month with clear-sky conditions and little significant fall/winter snow accumulation. During that time of the year, the air temperature drops significantly after sunset at the high-elevation Yellowstone National Park (averaging 2400 m) and the ground surface temperature decreases to near or below freezing accentuating the temperature contrast between hydrothermal areas and surrounding cooler areas. The night TIR image acquisition flights, planned after 11:00 p.m. typically lasted 3 to 4 h. While the coldest air and surface temperatures typically occurred near sunrise, flights were not scheduled at that time because of the formation of dew and increased water vapor over the hydrothermal pools. Therefore, acquisition times were scheduled before significant thermal fog formed and hours after sunset to minimize latent solar heat.

The monitoring effort involved image acquisition of high-priority hydrothermal areas such as NGB, and HSB. The flight lines provided an

Table 2
Characteristics of kinetic temperatures for NGB locations.

Name	Approximate kinetic temperature (Celsius)	Water body area (m^2)	Comments
Cinder pool	90	162	Steam bubbles mix pool.
Unnamed pool	76	92	Calm pool with minor outflow.
Hydrothermal explosion crater	30	1634	Carbon dioxide gas mixes pool.
The reservoir	30	4815	Carbon dioxide gas mixes pool.
Nuphar lake	10	7715	Cool water lake with no surface hydrothermal input.
Ground Temperature 1	32	Not applicable	
Ground temperature 3	24	Not applicable	

overlap of 30% among images in parallel lines. The FLIR SC640 camera had a focal plane array, uncooled microbolometer sensor that delivered an IR resolution of 640 × 480 pixels. Determining appropriate flight altitude was essential for acquiring 1-m pixel resolution images with the 40° field-of-view camera lens. Typically, the aircraft was approximately 1800 m above ground level (AGL) for safe night flying and for obtaining the 1-m pixel resolution. The ThermoVison ExaminIR, version 1.10.2 software controlled the FLIR camera. Capture of digital images happened at a frequency of 5 frames a second and storage of digital images was in sequential (SEQ) digital format. Prior to acquiring the first images, the aircraft flew down the center of the hydrothermal area so that the lens focus guaranteed crisp, high-spatial resolution TIR images. The FLIR SC640 camera was set to acquire imagery in the −40 to 120 °C range.

September or March image acquisitions may have included a single day flight to obtain shortwave 3-band MS imagery and LIDAR and a night flight for TIR imagery. Day flights occurred between solar noon and mid-afternoon under clear skies, usually the hottest time of the day. The day MS images (1-m pixel resolution) formed the calibrated 3-band orthomosaics and served as a base image for map-to-map rectification of the night TIR imagery. When the LIDAR was used, the aircraft was approximately 700–800 m AGL, resulting in high-resolution MS imagery varying from 0.2 to 0.4 m pixel sizes.

2.3. Image processing

Correcting the MS images for lens vignetting effects (Neale & Crowther, 1994) and for lens radial distortions (Sundararaman & Neale, 1997) as well as registering 3-band images for georectification were the initial steps. The HSB MS images from the September 2007 acquisition were rectified to a 2008 NSF Earthscope LIDAR topographic base. The 2008–2012 HSB night TIR images were map-to-map rectified with the georectified 2007 HSB MS image. The NGB MS images from the September 2008 acquisition were rectified to a 2008 NSF Earthscope LIDAR topographic base. This 2008 NGB georectified MS base was used in the map-to map rectification of the 2009 night TIR. The NGB MS image from 2010 was georeferenced directly to the USU LIDAR and formed the base map for the NGB 2010, 2011 and 2012 night TIR. Rectifying the USU airborne MS images to the georectified base map involved a 3rd order polynomial transformation. The root-mean-square error (RMSE) for all image rectification for all years was kept to less than 1-m. Assembling the image strips involved sub-setting and mosaicking of rectified images along the flight lines. Calibration of these image strips to a reflectance standard involved using the system calibration through a similar procedure described by Neale and Crowther (1994). A standard reflectance panel with known bi-directional properties (Jackson, Clarke, & Moran, 1992) was set up in a

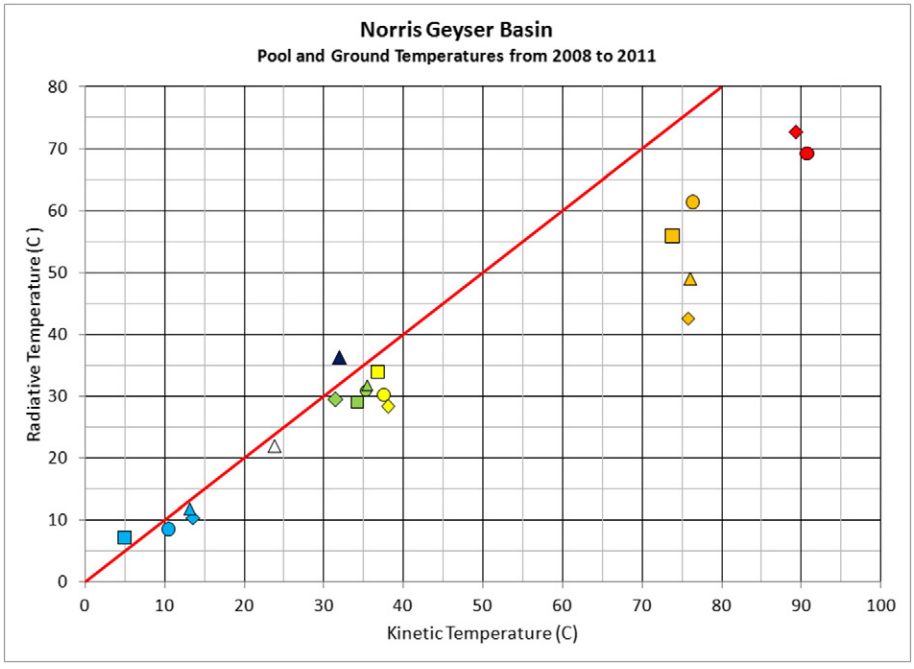

Fig. 4. Graph showing comparison of kinetic and radiative temperatures for 2008 (circles), 2009 (diamonds), 2010 (squares) and 2011(triangles) TIR image acquisitions. Red diamonds refer to temperature data for Cinder Pool, orange diamonds refer to an unnamed pool, yellow diamonds refer to the hydrothermal explosion crater, green diamonds refer to the Reservoir, light blue diamonds refer to Nuphar Lake, the black triangle refers to Ground Temperature 1, and the white triangle refers to Ground Temperature 3. See Fig. 3 for locations of temperature measurement sites.

Table 3
Spatial offsets of hydrothermal features in NGB using simple difference images and the 2010 visible orthomosaic (see text for discussion).

NGB location	Difference map	Feature	Offset (m)
Porcelain basin	2010–2011	Blue pool	6
Porcelain basin	2010–2011	Blue pool	4–5
Porcelain basin	2010–2011	White sinter	5–6
Unnamed pool	2010–2011	Pool	5
Scummy pool	2010–2011	Pool	3–4
Ledge spring	2010–2011	Pool	1-2m
HE crater	2010–2011	Pool	4
Pearl geyser	2011–2012	Geyser	5
Grey lakes channel	2011–2012	Hydrothermal stream	4–5
Porkchop geyser	2011–2012	Geyser	4
NE thermal activity	2011–2012	Pools; geysers	5
Second erupter	2011–2012	Geyser	5
Steamboat geyser	2008–2009	Geyser	5
Steamboat geyser	2009–2010	Geyser	5–6
Steamboat geyser	2010–2011	Geyser	1
Steamboat geyser	2011–2012	Geyser	7

central location during the flight, overlooked from nadir by an Exotech radiometer with Thematic Mapper bands (similar to the airborne digital cameras of green (0.55 μm), red (0.67 μm) and near-infrared (0.8 μm). The radiometer measured incoming irradiance from the sun and sky every minute, which was then used to calibrate the image strips in terms of reflectance. The location of the standard reflectance panel setup was either at the Old Faithful area in Yellowstone National Park or at the West Yellowstone, Montana, airport. Once calibrated, stitching the rectified image strips together produced a mosaic for each hydrothermal area. The calibrated, 3-band orthomosaics formed the base map for rectification of the night TIR imagery and were used to calculate an emissivity layer for each area. One emissivity layer was used for all years, based on the day high-resolution mosaic (base image) which was used to estimate the Normalized Difference Vegetation Index (NDVI) for the fraction of cover scaling in the emissivity calculations.

Prior to image processing, extraction of individual TIR images from the native format SEQ files at approximately 60 to 70% overlap along the flight line occurred. Standardization of the image extraction procedure using the ExaminIR software included setting variables and parameters the same for all flights: the emissivity was set to 1, the background air temperature to 0 °C with a relative humidity of 10%, and a temperature of the external optics of 10 °C and transmissivity of 1.

Visual rectification of the individual TIR images to the 3-band MS orthomosaic involved the use of common ground control points. Stitching individual TIR images together along the flight lines created the night TIR image strips. The formation of a night TIR mosaic for a hydrothermal area entailed the mosaicking of several calibrated strips from parallel flight lines. These visually rectified TIR night mosaics may have an offset ~5–6 m from the same hydrothermal features on the orthorectified visible mosaic.

Correction of the at-aircraft temperature image mosaics for atmospheric transmission effects included the application of the MODTRAN (MODerate resolution TRANsmission) radiative transfer model (Berk, Bernstein, & Robertson, 1989). Radiosonde data collected in Great Falls, MT at 0 and 12 GMT provided the profile of temperature and humidity between the surface and the aircraft altitude, required as input data by the model. Because Great Falls is at lower elevation than the hydrothermal areas in YNP, only the portion of the profile starting at the corresponding elevation and anchored with the dew point temperature data from local surface weather stations within the Park was necessary. MODTRAN was run multiple times for the atmospheric profile and for different surface emissivity, ranging between 0.90 and 0.98. A regression line enabled the adjustment of airborne radiometric temperatures in the image according to surface emissivity and the atmospheric profile at the time of the flight.

The technique proposed by Brunsell and Gillies (2002) afforded an estimate of surface emissivity. The scaled (NDVI) obtained from the calibrated 3-band image mosaic yielded a fraction of vegetation cover layer for linear scaling the emissivity of the surface between minimally vegetated sinter (0.90), and full canopy /dense vegetation cover (0.98). The ERDAS Imagine software processed all imagery. The application of the NDVI to the calibrated 3-band image mosaic for generation of image layer utilized the following equation:

$$NDVI = (NIR - Red)/(NIR + Red) \quad (1)$$

Scaling the NDVI yielded the N* parameter in raster form:

$$N* = (NDVI - NDVI_0)/(NDVI_{max} - NDVI_0) \quad (2)$$

where $NDVI_0$ is the bare soil NDVI value of the scene and $NDVI_{max}$ is the maximum NDVI of the scene corresponding to full cover dense vegetation. The fraction of vegetation cover (Fr) became:

$$Fr = N*^2 \quad (3)$$

Linear scaling the emissivity between bare sintered soil ($\varepsilon_{soil} = 0.90$) and full dense vegetation cover ($\varepsilon_{veg} = 0.98$) using the Fr image layer produced the surface emissivity layer:

$$\varepsilon_{surf} = Fr\ (\varepsilon_{veg}) + (1 - Fr)\ \varepsilon_{soil} \quad (4)$$

Applying equations 1 through 4 to the calibrated MS 3-band mosaic, using the at-aircraft radiometric temperature mosaic and the developed temperature correction from MODTRAN, an ERDAS Imagine model generated a spatial surface emissivity layer. Assigning an emissivity of 0.985 to water surfaces in the scene involved the identification of water using

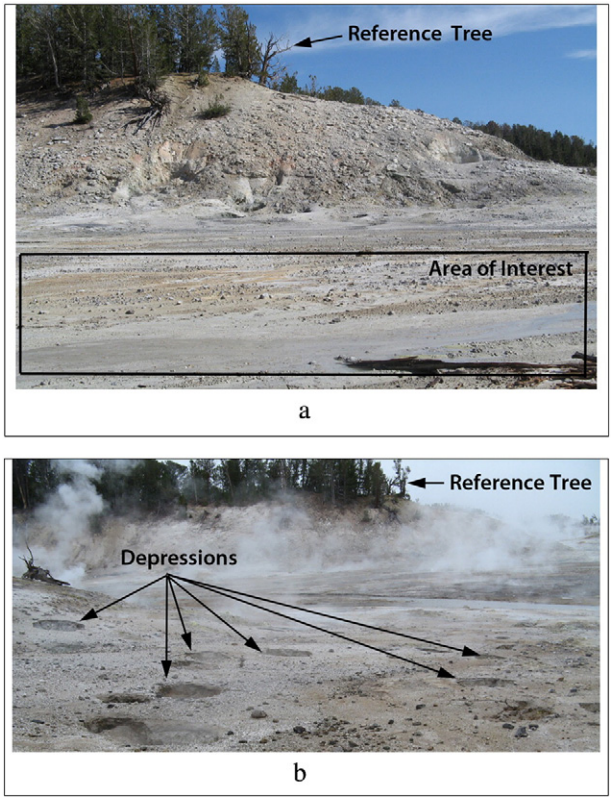

Fig. 5. a–b. Photographs showing north end of Main Basin for 26 August 2007 and 4 September 2008. Although the photographs are from a different perspective, the numerous new depressions and hydrothermally altered ground was a significant difference between 2007 and 2008. There is a reference tree for comparison of the two images. View looking south.

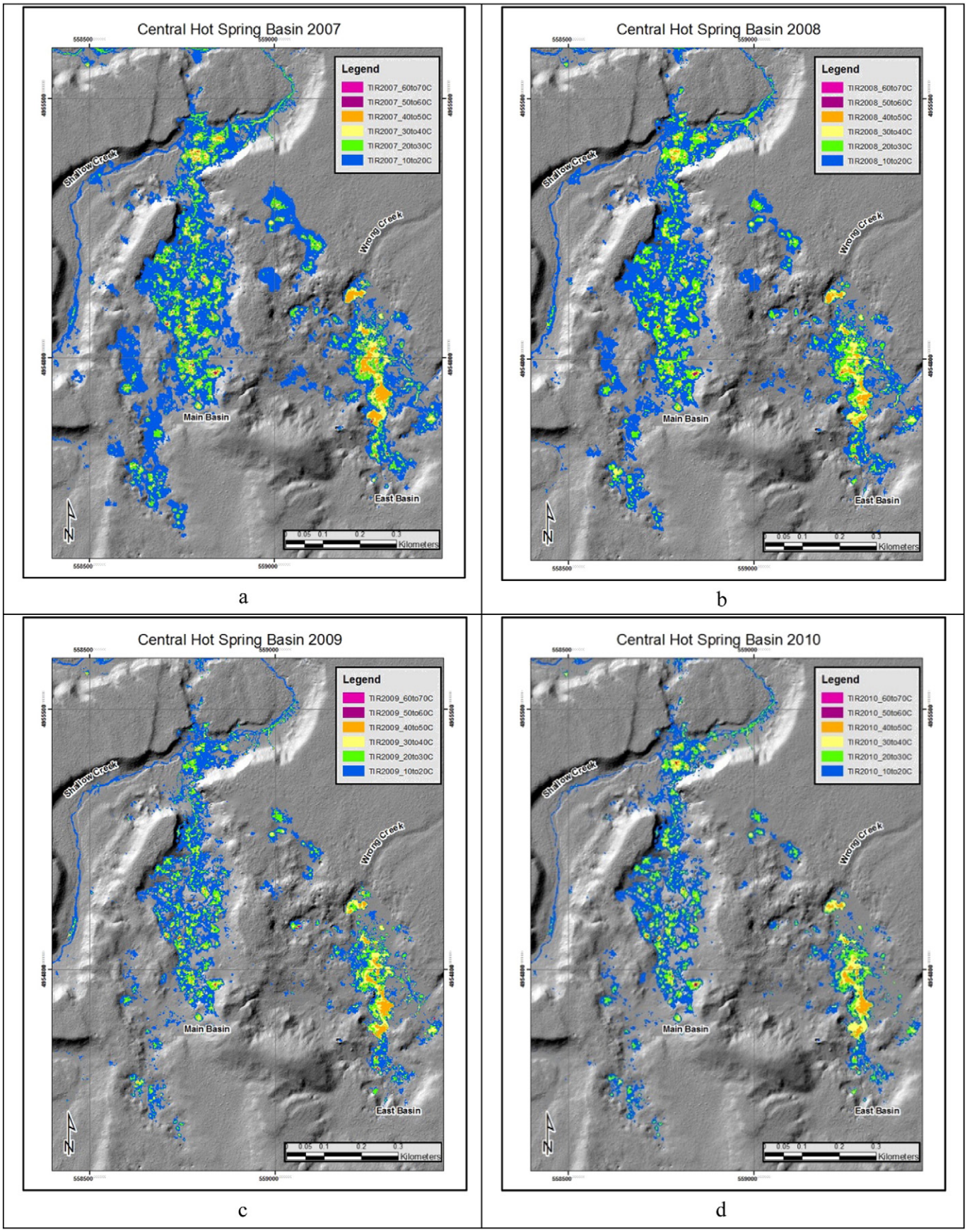

Fig. 6. a–d. Night TIR radiometric temperature maps showing temperature components of the central HSB hydrothermal system with its N to S-trending hydrothermal basins for September 2007 (a), 2008 (b), 2009 (c) and 2010 (d). NSF Earthscope 2008 LIDAR base map (shaded grey) available at www.opentopography.org accessed 10 September 2014. TIR imagery available at www.mbmg.mtech.edu/gis/gis-ArcGISservices.asp, accessed 28 September 2015.

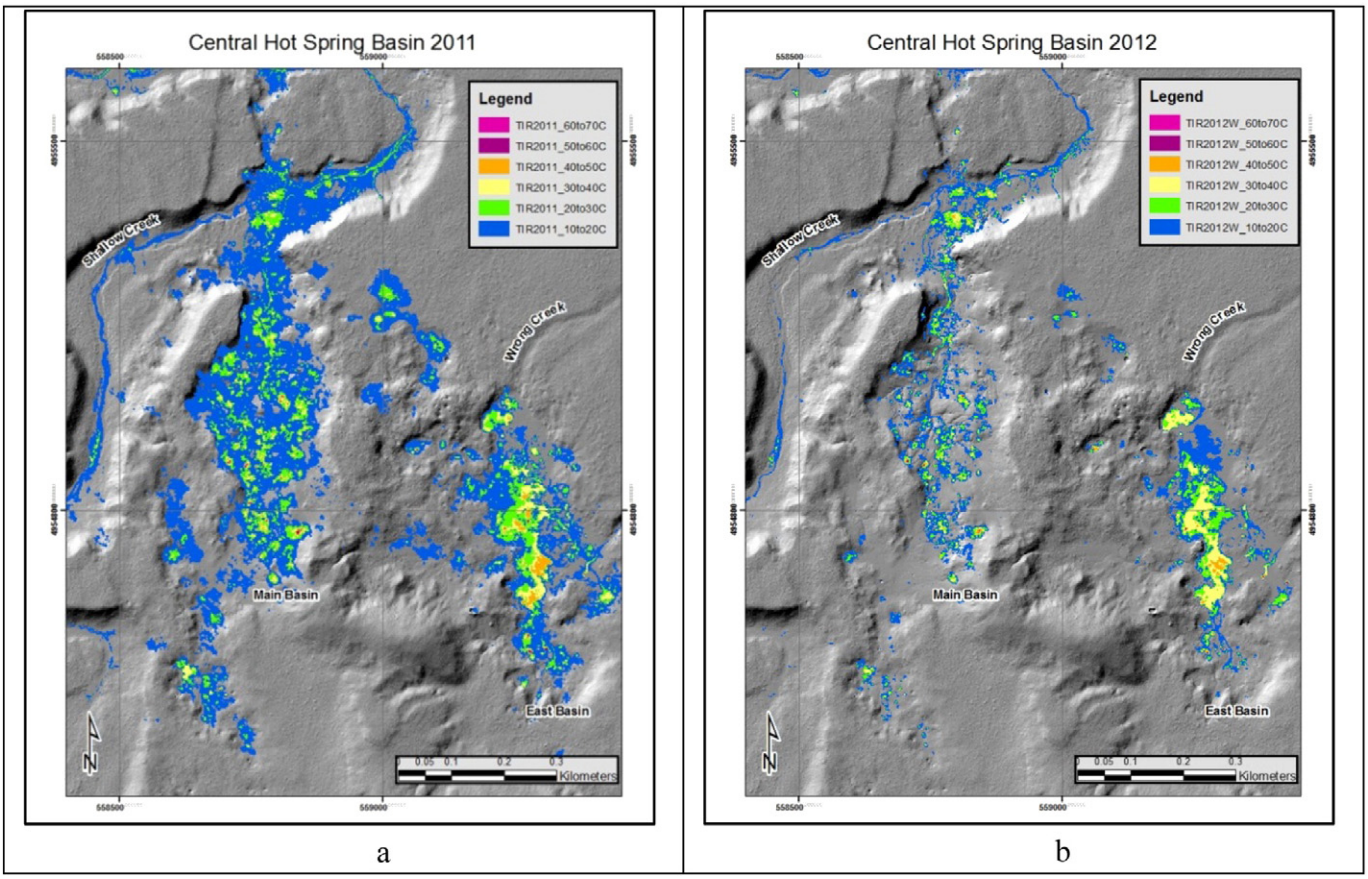

Fig. 7. a–b. Night TIR radiometric temperature maps showing temperature components of the central HSB hydrothermal system with its north-south trending hydrothermal basins for September 2011 (a), March 2012 (b). NSF Earthscope LIDAR 2008 base map (shaded grey) available at www.opentopography.org accessed 10 September 2014. TIR imagery available at www.mbmg.mtech.edu/gis/gis-ArcGISservices.asp, accessed 28 September 2015.

spectral classification of the high-resolution calibrated 3-band image to produce a spatial water body mask. The model output is an at-surface radiometric temperature image layer corrected for atmospheric effects and surface emissivity.

3. Assessment of thermal infrared technique

For NGB and HSB, ground-based (in-situ) temperature data provided an assessment of the TIR technique's precision and accuracy. A comparison of the highest radiative temperature for all years of image acquisition is one measure of the consistency of the estimated radiative temperatures for each hydrothermal system. The accessibility of NGB enabled a comparison of measured ground and pool kinetic temperatures with the calculated radiative temperatures. Additionally, a qualitative assessment of spatial accuracy for processed TIR imagery at NGB offered useful constraints for geologic applications.

3.1. Consistency of calculated radiometric temperatures

The maximum radiative temperature within the corrected TIR images is an indication of consistency of the night TIR image acquisition. At different dates and times, the highest temperatures of a hydrothermal system should approach 90 to 92 °C- the boiling temperature of water at the average elevation (2400 m) of Yellowstone. It is reasonable that the corrected, airborne TIR temperatures are less than the maximum kinetic temperatures because water vapor masks the actual surface temperatures of high-temperature hydrothermal ground or pools. However, the maximum radiative temperatures derived from the TIR imagery, although less than boiling, should be similar due to water vapor above the hottest pools.

A summary of basic image information (Table 1) for the two hydrothermal systems- HSB and NGB-highlights the date/time of night TIR image acquisitions and the air temperature near ground level for 2007 through 2012. The meteorological station located at the Lake Water Tank (http://ard-request.air-resource.com, accessed 17 September 2014) provided air temperatures for the HSB comparison and the YNP Geology Program Onset temperature logger at the Norris Museum for NGB provided air temperatures for the NGB assessment. For HSB TIR imagery, the maximum average radiative temperature (Table 1) is 63.93 °C with a standard deviation of 6.8 °C. For NGB TIR imagery, the average maximum radiative temperature is 70.37 °C with a standard deviation of 4.5 °C. Not surprisingly, atmospheric conditions were not identical from year to year and the air temperatures at the time of the flight indicate this variability. The similarity of the maximum calculated radiative TIR image temperature implies consistency in the image processing technique.

Fluctuations in radiometric ground temperature demonstrated that the 2009 night TIR acquisition occurred near the time of minimum residual solar heating (Fig. 2). At NGB, a hydrothermal explosion crater contained an experiment for measuring the variable residual solar heating (Fig. 3). An infrared radiometer mounted on a pole and pointing at hot, dry hydrothermal ground measured the daily fluctuations during the 10 September 2009 image acquisition. The ground surface temperatures reached a minimum around 6:00 a.m., close to the minimum air temperature, and then increased after sunrise reaching a peak around 2:00 p.m. Flights typically occurred between midnight and 4:00 a.m. Fig. 2 indicates that low ground surface temperatures, varying

between 2 and 4 °C above the minimum temperature, occurred during the 2009 night TIR acquisition. The amount of solar heating and radiative cooling varied according to atmospheric conditions during the previous day: cloud cover, precipitation, and air temperature. Future investigations will address and correct for this known effect within the airborne, radiative temperature images.

3.2. Comparison of kinetic and radiative temperatures

The accessibility and dynamics of the hydrothermal system at NGB allowed an assessment of the derived radiative and measured kinetic temperature's accuracy. Surface kinetic temperatures measured at different ground locations provided ground truth for an assessment of radiative temperatures derived from the corrected and calibrated airborne 2008 to 2011 TIR imagery. Five water bodies of varying size and kinetic temperatures (Fig. 3) contained temperature sensors during the times of the night TIR flights. In 2011, two additional sites (Fig. 3) had temperature sensors measuring ground temperatures during the night TIR flight.

Onset Computer Corporation temperature loggers measured kinetic surface temperatures using two types of loggers: the Onset Hobo Pro and the Onset Microstation. Both loggers had 2-m length thermistor probes, accurate to within 0.2 °C. Placement of loggers for water body temperatures involved inserting the thermistors approximately 1 to 5 cm below the water surface and approximately 1.5 m from the shoreline. For ground temperatures, placement of thermistors involved their burial 1 cm below the ground surface. Both the water body and ground temperature loggers acquired temperature data at 1-min intervals. Thermistors were placed at hydrothermal pools with well-mixed temperatures and hydrothermally active ground (Table 2; Fig. 4). For each

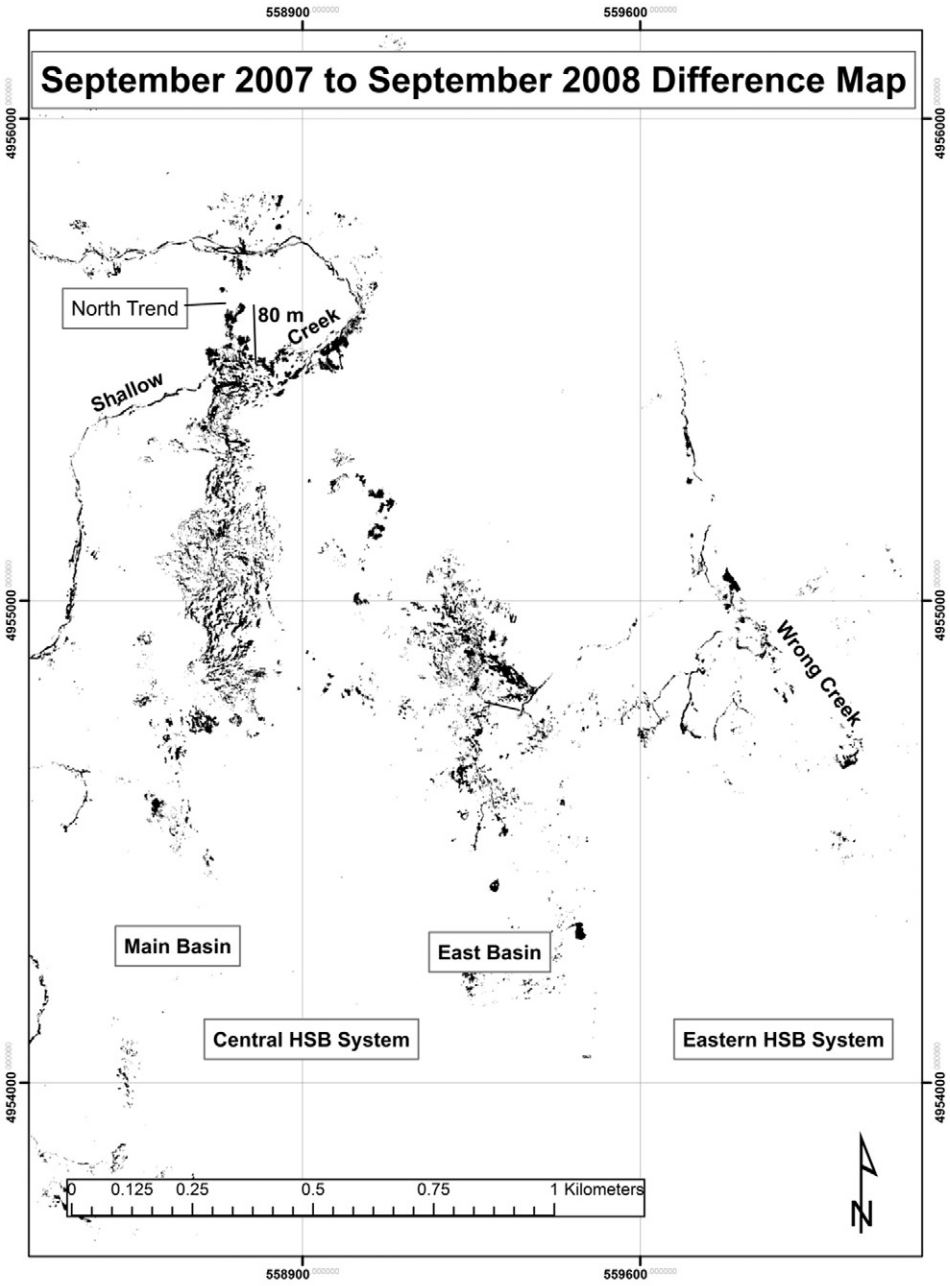

a

Fig. 8. a–c Simple difference maps for September 2007–2008, September 2010–2011 and September 2011 to March 2012 for HSB. The dark areas on the map indicate large magnitude and positive differences in temperature. The white area represents little or no change.

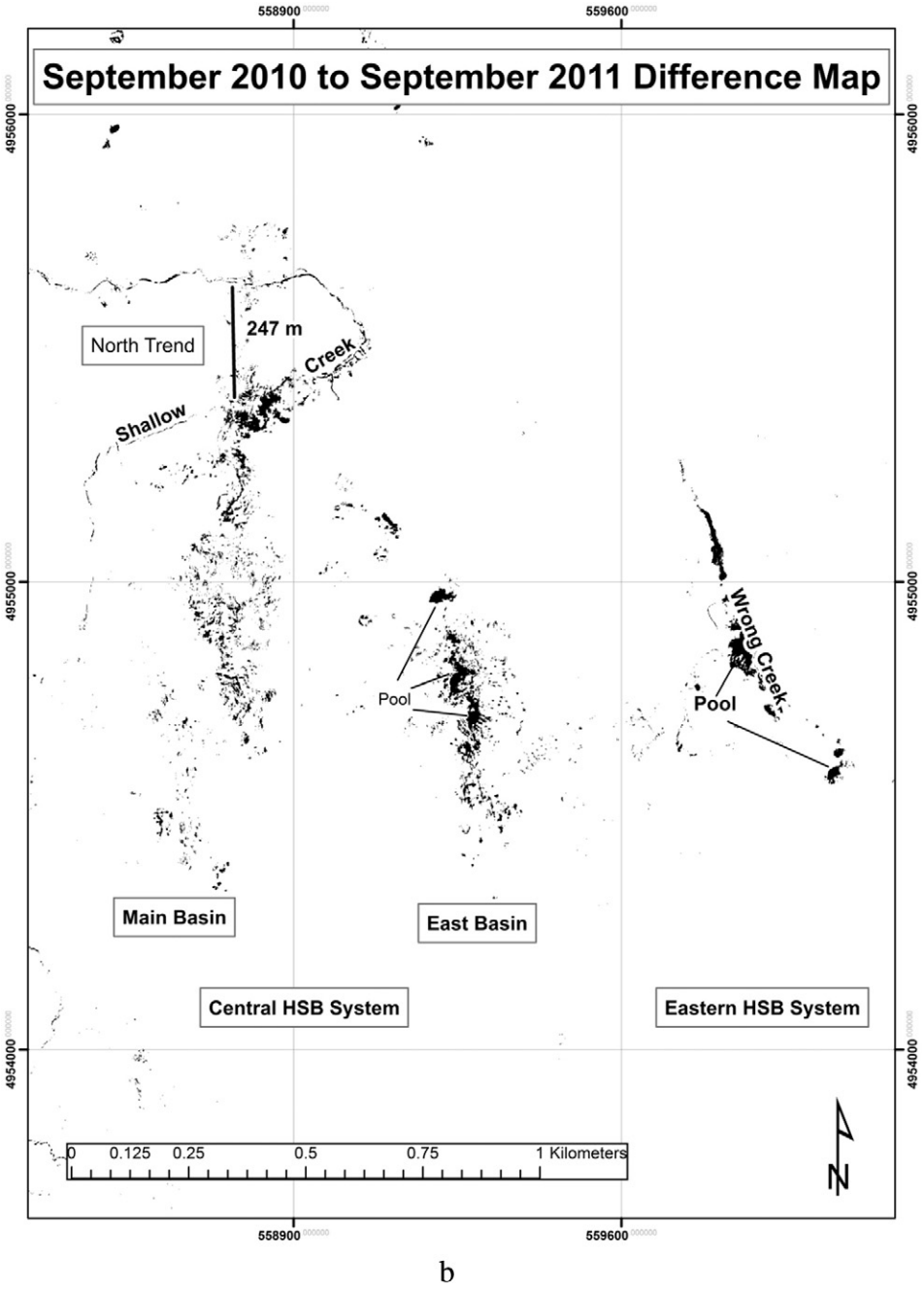

b

Fig. 8 (*continued*).

measurement site (Table 2), the approximate, measured ground kinetic temperature, the area of the water bodies, and the associated comments provide additional information on the sites chosen for this assessment.

Hydrothermal pools of different temperatures enabled an assessment of the difference between calculated values of at-surface, radiative temperatures and measured kinetic ground temperatures. For three of the selected pools, bubbling gases (steam or carbon dioxide) mixed the hydrothermal waters at Cinder Pool, the Reservoir and the hydrothermal explosion crater thus providing a pool with a near-constant temperature.

Comparison of calibrated and corrected TIR temperatures (2008 through 2011) with the measured kinetic temperatures yielded an assessment of the airborne technique's temperature accuracy. The GPS coordinates of the thermistors provided a location for selecting representative radiative temperatures from the night TIR image. The maximum calculated value of radiative temperature over a 4 pixel (4 m^2) area provided an estimate of radiative temperature. An area of 4 pixels accounted for positional inaccuracies during the production of the night TIR image mosaic. The 1-min, ground temperature data recorded during airborne acquisitions provided kinetic temperatures for comparison with calculated surface values of radiative temperatures. Results of the temperature comparison (Fig. 4) showed that kinetic and radiative temperatures generally agreed for temperatures less than 35 °C. For kinetic temperatures greater than 35 °C, the root mean square error for the relationship is 19.1 °C with a mean bias error of −16.8 °C. For kinetic temperatures <35 °C, the root mean square error is 3.3 °C with a mean bias error of −1.8 °C.

At high temperatures, water vapor associated with hydrothermal pools is the most likely explanation for the lack of agreement between the measured kinetic and derived radiative temperatures. At the time

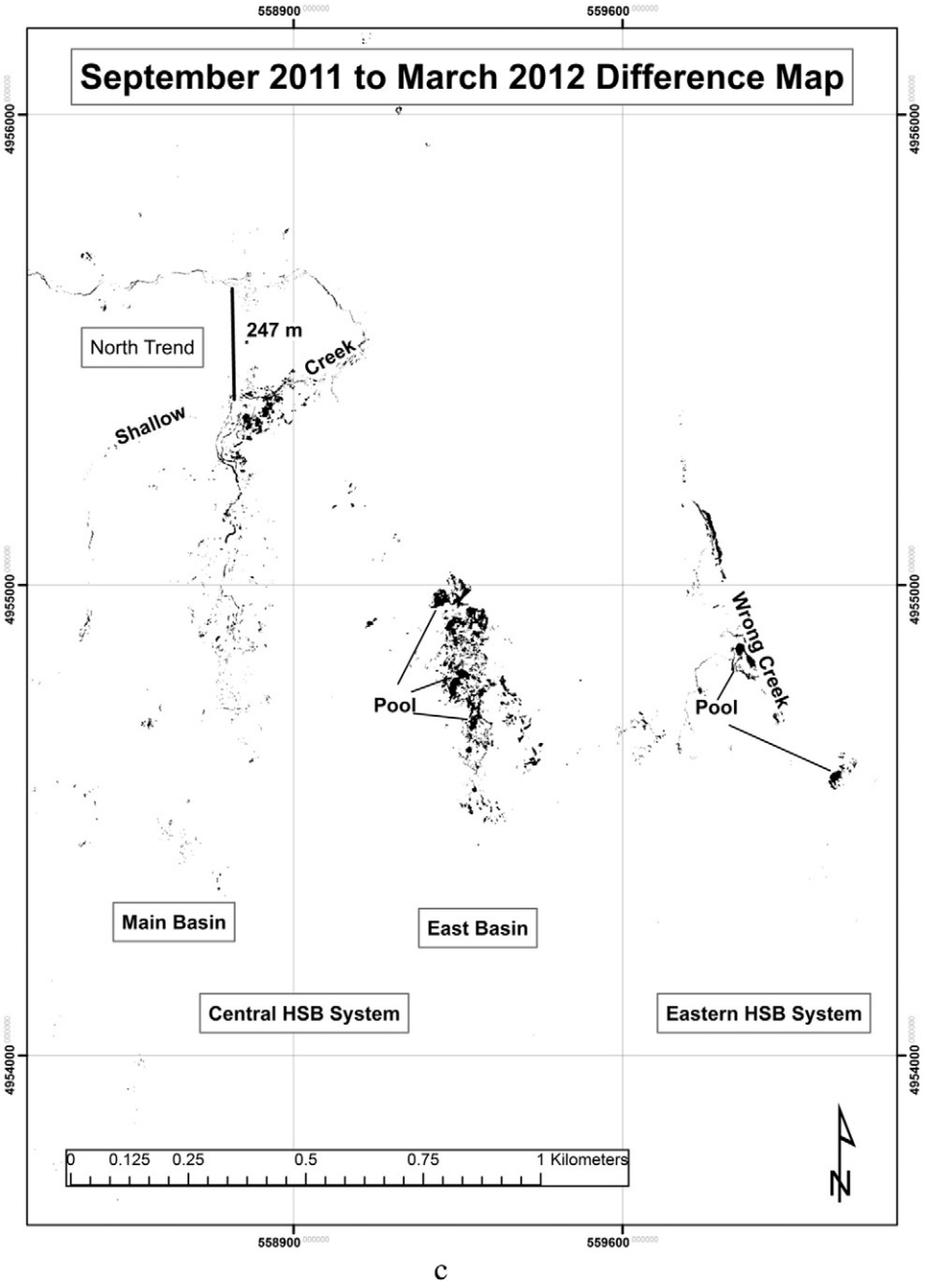

Fig. 8 (*continued*).

of the flights, the air temperature at NGB ranged from −3.1 to 6.9 °C. The relatively low-air temperature and the high-pool temperatures can cause a zone of water vapor above the pool and may lead to the formation of a water vapor cloud. Because water vapor absorbs the 8 to 12 μm TIR energy, the calculated, radiative at-surface temperatures are less than the measured kinetic, surface temperatures due to the presence of a water vapor cloud.

For their study in Alaska, Haselwimmer, Prakash, and Holdmann (2013) reported that airborne radiometric temperatures at Pilgrim Hot Springs consistently underestimated ground kinetic temperatures by ~2 to 3 °C. However, the maximum temperatures for their study were 58 °C, well below the 75 °C to 91 °C measured in this study. Thus, Haselwimmer et al. (2013) encountered few problems associated with water vapor absorbing the TIR energy at high temperatures.

3.3. Assessment of spatial accuracy

For the 2008 to 2012 night TIR mosaics, a qualitative assessment of spatial accuracy involved NGB's boardwalks and trails as well as individual hydrothermal features scattered throughout the simple difference maps of night TIR mosaics. An easily identified trail junction on the 2008–2012 TIR mosaics showed a spatial variation ranging from 2 to 6 m. The 2–6 m spatial variability provides a qualitative estimate of spatial offsets between the 2010 visible orhtomosaic and the 2008–2012 night TIR mosaics. Comparing hydrothermal features on the 2010–2011 and 2011–2012 NGB simple difference maps (Table 3) also suggested a spatial offset (1–7 m) between hydrothermal features in the visible mosaic and the same hydrothermal features in a basin-wide change detection map (see Section 4.2 for additional details). For the 2010–2011 simple difference map, Steamboat Geyser showed a 1 m

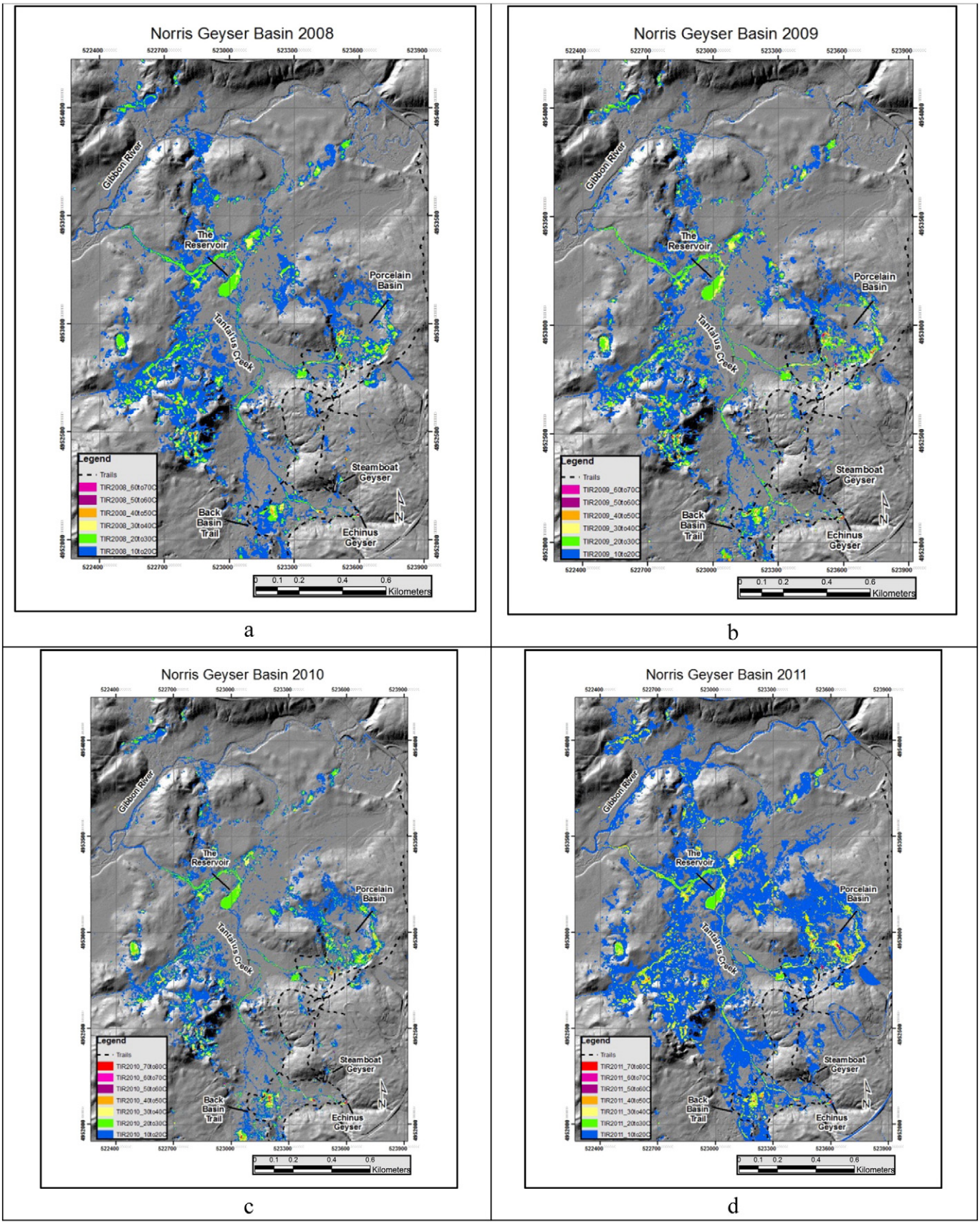

Fig. 9. a–d. Night TIR radiometric temperature maps showing temperature components of NGB hydrothermal system for September 2008 (a), 2009 (b), 2010 (c) and 2011 (d). USU 2010 LIDAR base map (shaded grey). LIDAR and TIR imagery available at www.mbmg.mtech.edu/gis/gis-ArcGISservices.asp, accessed 28 September 2015. e. Night TIR radiometric temperature maps showing temperature components of NGB hydrothermal system for March 2012. USU 2010 LIDAR base map (shaded grey). LIDAR and TIR imagery available at www.mbmg.mtech.edu/gis/gis-ArcGISservices.asp, accessed 28 September 2015.

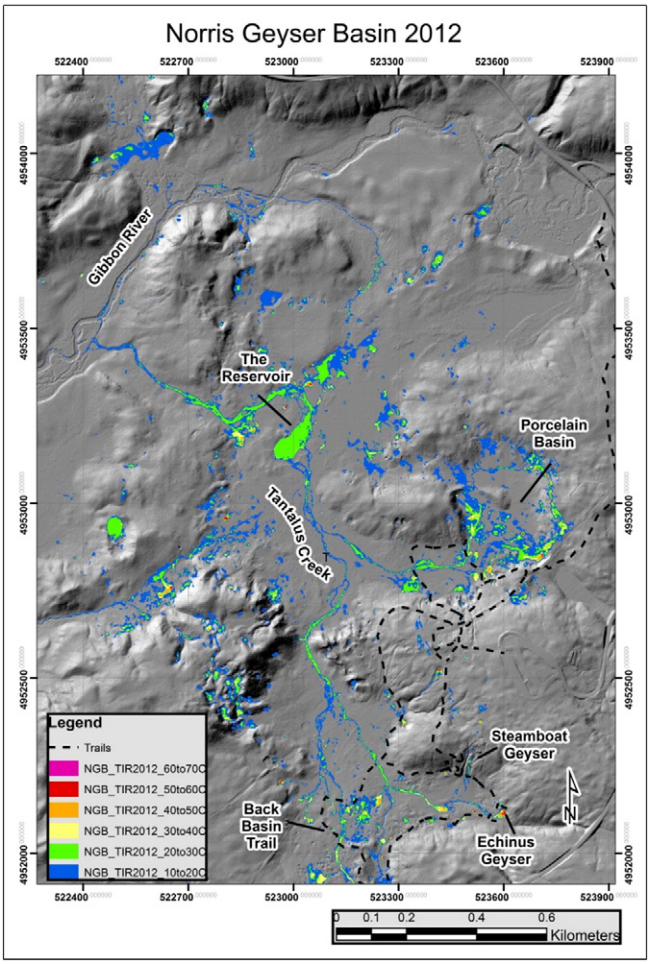

e

Fig. 9 (*continued*).

offset between the 2010 orthorectified visible mosaic and the 2010–2011 TIR simple difference maps. However, for the 2011–2012 TIR simple difference map, Steamboat Geyser showed a 7 m spatial offset. Within NGB, the visible-TIR contrast between an individual hydrothermal feature on the day visible mosaic and the night TIR mosaic is small and varies from year to year. However, the strong visible-TIR contrast between the asphalt NGB parking lot and the vegetation is distinct and consistent from year to year resulting in a ~1 m spatial location error. Given the difficulty and time-intensive effort in consistently identifying the same hydrothermal location within 1 m between the day visible imagery and the night TIR, it is not surprising that spatial offsets do occur between sequential night TIR image acquisitions. Thus, the challenge still remains to visually and consistently tie night TIR imagery to an orthorectified visible mosaic for NGB and other hydrothermal areas with few stable ground control points.

4. A new perpsective of the Hot Spring Basin and Norris Geyser Basin hydrothermal systems

These two hydrothermal systems illustrate challenges associated with the development and application of this airborne TIR monitoring technique. First, there is a contrast between the accessibility of HSB and NGB that is important to mention. Dynamic changes in the NGB hydrothermal system were less difficult to confirm than changes in the HSB hydrothermal system primarily because NGB is accessible year-round using wheeled vehicles or over-the-snow vehicles whereas the remote HSB can require two days of summer hiking to access or a week-long winter expedition in an area managed as wilderness. While images of both hydrothermal systems can be acquired by remote sensing techniques, ground confirmation of changing hydrothermal conditions required a substantially greater investment of time and resources for the HSB hydrothermal system than for the NGB hydrothermal system. Yet, both hydrothermal systems are dynamic and important for documenting changes in hydrothermal activity and the hydrothermal system's natural variability. The following sections present a time-sequence for HSB (2007 to 2012) and for NGB (2008 to 2012) that has documented changing hydrothermal activity, natural variations, limitations of this remote sensing technique, as well as the potential for the hydrothermal monitoring of these dynamic natural systems. Temperature maps and simple change detection maps have provided both qualitative and quantitative estimates of changes within the HSB and NGB hydrothermal systems. Temperature maps are “snapshots” of hydrothermal temperature patterns for HSB (2007–2012) and NGB (2008–2012). The temperature maps also are a proxy for the heat from these hydrothermal systems. Simple change detection algorithms were used to quantify changing hydrothermal activity by systematically and uniformly calculating magnitudes of temperature changes.

4.1. Hot Spring Basin

Field observations at HSB in 2007 and 2008 focused attention along a N-trending fracture/fault system. During 2007 fieldwork, laminated and compacted sediments along Shallow Creek (Fig. 5a) were observed. In 2008, the same area along Shallow Creek had become “pockmarked” and the ground was hydrothermally altered (Fig. 5b). Jaworowski, Heasler, Neale, Sivarajan, and Masih (2013) identified changes in HSB night TIR imagery that were consistent with the field observations shown in Fig. 5. It is interesting to note that these changes, both ground observations and airborne TIR, in the HSB hydrothermal system occurred during rapid uplift of the Sour Creek resurgent dome (Dzurisin, Wicks, & Poland, 2012; Chang, Smith, Wicks, Farrell, & Puskas, 2007).

The time-sequence of night TIR imagery (Figs. 6a–d, 7a–b) for the HSB hydrothermal system (2007–2012) documented the natural variability of temperature and fluid-flow within this fracture-dominated system as well as changing hydrothermal activity. Major N-S trending basins (Main Basin and the East Basin), alignments of hydrothermal features in the night TIR imagery and the terrain lineaments show the hydrothermal system's fracture permeability through the Lava Creek Tuff and overlying sediments.

Simple difference maps between annual image acquisitions (September 2007–September 2008 and September 2010–September 2011) and the first seasonal image acquisition (September 2011–March 2012) have provided maps of the hydrothermal changes and demonstrated the usefulness of simple change detection as a hydrothermal monitoring technique. The simple difference map generated between the September 2007 and September 2008 night TIR acquisitions shows temperature changes along an approximately 80 m length (Fig. 8a) in the Main Basin of the HSB hydrothermal system. This change in hydrothermal activity is less evident in the individual temperature maps shown in Figs. 7a or 7b. Similarly, the simple difference map generated between the September 2010 and September 2011 TIR acquisitions shows the fumarolic activity in the Main Basin, the hydrothermal pools in the East Basin and the north-northwest (NNW) trending hydrothermal pools along Wrong Creek (Fig. 8b). However, there is only discontinuous hydrothermal activity along a 247 m North trend from September 2010 to September 2011. In contrast, while showing similar discontinuous North-trending hydrothermal activity along 247 m, the simple difference map generated between the September 2011 and March 2012 acquisition Fig. 8c) primarily shows large-magnitude temperature change (positive) within the hydrothermal pools of the East Basin and the NNW-trending hydrothermal pools along Wrong Creek. On the September 2011–March 2012 simple difference map, the high-elevation and snow-covered March 2012 landscape may be a reason for the apparent lack of hydrothermal activity along the N-trending

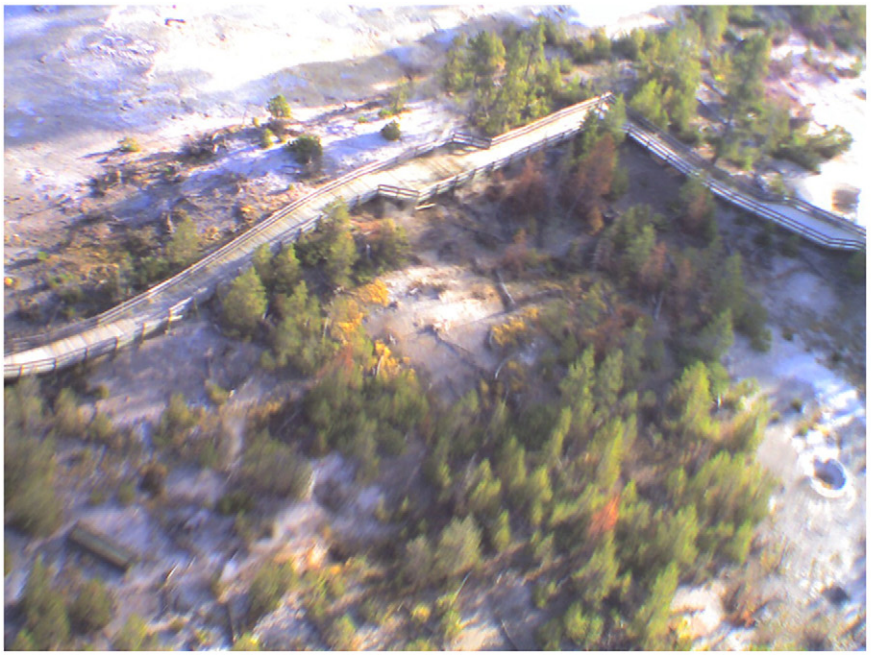

a

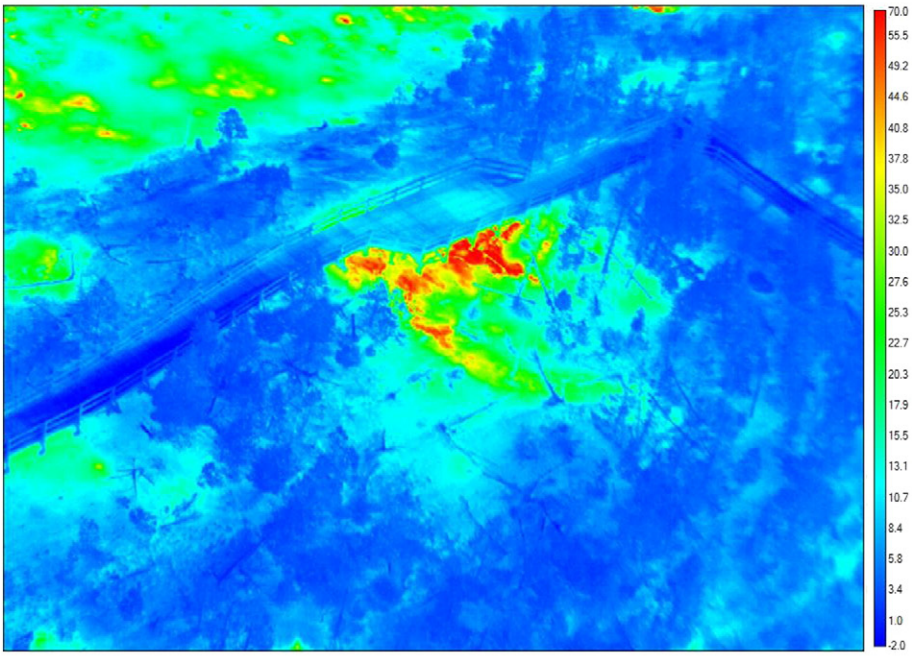

b

Fig. 10. a. Helicopter-oblique aerial photograph showing area of Back Basin hydrothermal activity on 10 September 2011. Notice the white, efflorescent ground and the dying trees centered on the "hot", wide boardwalk near the upper center of the photograph. View looking north. b. Helicopter-oblique aerial photograph showing the same area of Back Basin hydrothermal activity on 10 September 2011 as shown in Fig. 11a. Notice the day TIR centered on the "hot" boardwalk and the rectangular area of hydrothermal activity south of the boardwalk. View looking north. Temperature scale on the right of the image is Celsius.

zone of discontinuous hydrothermal activity (labeled North Trend in Fig. 8) between the east (E)-flowing and west (W)-flowing reaches of Shallow Creek.

4.2. Norris Geyser Basin

Natural fractures within the 640,000 year-old Lava Creek Tuff control hydrothermal fluid flow within the NGB hydrothermal system (Jaworowski, Heasler, Hardy, & Queen, 2006) and the night TIR imagery reflects changing hydrothermal fluid flow along NW and NE-trending fractures as well as N to S and E to W-trending fractures (Fig. 9a–e). NGB is an unusual hydrothermal system in Yellowstone because a single NW-flowing creek, Tantalus Creek (green colors 20 °C to 30 °C and blue 10 °C to 20 °C), captures 98% of the thermal discharge of NGB (Friedman, 2007) and flows into the sinuous Gibbon River (10 to 20 °C). The temperature components (10 °C to 70 °C; blue to red) show the preferred orientation of hydrothermal fluid flow along NE- and NW-trending fractures. Tantalus Creek flows through the Reservoir, a hydrothermal feature consistently between 20 and 30 °C. When erupting, numerous geysers, including the impressive Steamboat Geyser, periodically expel

hot water and steam that may be seen as hydrothermal outflow on night TIR mosaics. Because NGB is a dynamic hydrothermal system and there is continual change in geysers, hot springs, and hydrothermally altered ground, the challenge is to document a physical change within a hydrothermal area that can improve the scientific understanding of the hydrothermal system.

Environmental differences between the acquisitions may be responsible for some variability in the temperature maps of the HSB and NGB hydrothermal systems. For example, the earliest flight time and warmest air temperature occurred during the September 2011 image acquisition resulting in a large area of 10 °C–70 °C temperatures for the HSB and NGB hydrothermal systems (See Figs. 7a for HSB and 9d for NGB). Thus, solar heating is one parameter that may have caused the warm background noticed during the 2011 image acquisition.

Between the 2011 and 2012 acquisitions, ground observations at two areas within NGB, the Back Basin and along the northeastern edge of Porcelain Basin (aka Porcelain Terrace), indicated changes in hydrothermal activity. During summer 2011, Yellowstone National Park geologists investigated a report of new hydrothermal activity in NGB's Back Basin (Heasler, Bueter, & Jaworowski, 2011). The following excerpt highlights the initial ground observations cited in Heasler et al. (2011):

> *In mid-June 2011, Norris Geyser Basin Interpretive staff talked with park geologists about new thermal activity along the Back Basin trail. The Norris Interpretive staff described the new thermal activity as near the boardwalk between Yellow Funnel Spring and Porkchop Geyser (Figs. 1, 2, 3). They reported a very sweet smell in the area where pine trees were turning brown and the ground was discolored.*

Yellowstone geologists visited the area from 16 July 2011 through 11 August 2011 to measure ground temperatures and geothermal gases. A FLIR SC640 Thermacam identified areas of the ground surface that were near the boiling temperature of water (93.3 °C at NGB). The measured subsurface temperatures (92.7 °C) indicated steam transport through fractured ground (Fig. 10a and b). Hydrothermal gas concentrations also indicated that gas was being forcefully emitted from a temperature-probe hole.

Increased hydrothermal activity also occurred along a n-trending fracture along the northeastern edge of Porcelain Basin (aka Porcelain Terrace) in NGB. No ground measurements (temperature or gas) were conducted along the ~137 m N-trending line of increased hydrothermal activity because of the unstable ground along Porcelain Terrace.

Documentation of the 2011 hydrothermal activity along the *N*-trending fracture occurred during a helicopter condition assessment over Porcelain Basin (Fig. 11). This increased hydrothermal activity continued at Porcelain Terrace and in the Back Basin through winter 2012.

Within the NGB hydrothermal system, simple difference maps (ENVI change detection algorithm) confirmed that the night TIR imagery detected a large magnitude (positive temperature change) of increased hydrothermal activity observed in the Back Basin and along Porcelain Terrace. The ENVI simple difference algorithm performed a difference between two images and displayed the magnitude of temperature change as an increase or decrease of temperature. The simple difference image (largest magnitude positive change in temperature class) between the night September 2010 and night September 2011 TIR imagery shows an oblong E-W trending area (107 m^2) approximately 10 m south of the Norris boardwalk within the Back Basin (Fig. 12). And the simple difference image (largest magnitude positive change in temperature class) between the night September 2011 and night March 2012 TIR imagery shows a N-trending (27 m^2) area was centered on the Norris boardwalk. These TIR simple difference patterns are consistent with the ground observations from August through September 2011. During the 2011–2012 winter, it is interesting to note that little to no snow accumulated on the Norris boardwalk in this area of high-heat flux. For Porcelain Terrace, the 2010–2011 simple difference

Fig. 11. Helicopter-oblique aerial photograph (10 September 2011) showing area of hydrothermal activity along the NE edge of Porcelain Basin i.e. Porcelain Terrace. Notice the N-trending columns of steam and the blue pool. View looking north.

image (largest magnitude positive change in temperature class) showed a NNW-trending area (3048 m^2) and the 2011–2012 difference image also showed a less spatially extensive NNW-trending area (938 m^2) of hydrothermal activity along Porcelain Terrace (Fig. 13a and b).

For the NGB and HSB hydrothermal systems the simple difference algorithms clearly delineated changes in the hydrothermal area for the

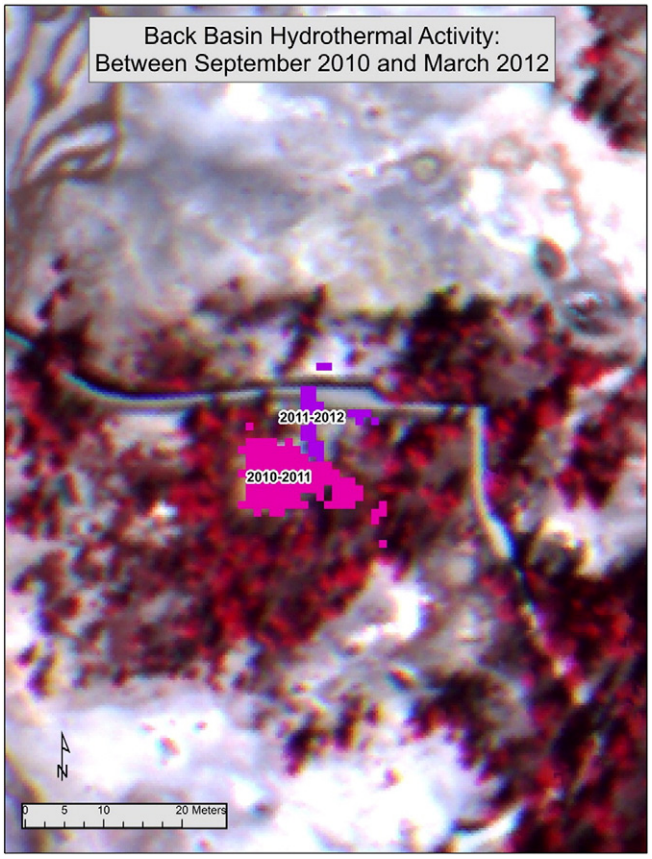

Fig. 12. Simple difference maps for September 2010–September 2011 and September 2011–March 2012 draped over the 2010 false-color orthomosaic. Notice the E-W trending hydrothermal pattern from 2010 to 2011 and the N-S trending pattern from 2011 to 2012. 2010 false-color orthomosaic available at www.mbmg.mtech.edu/gis/gis-ArcGISservices.asp, accessed 28 September 2015.

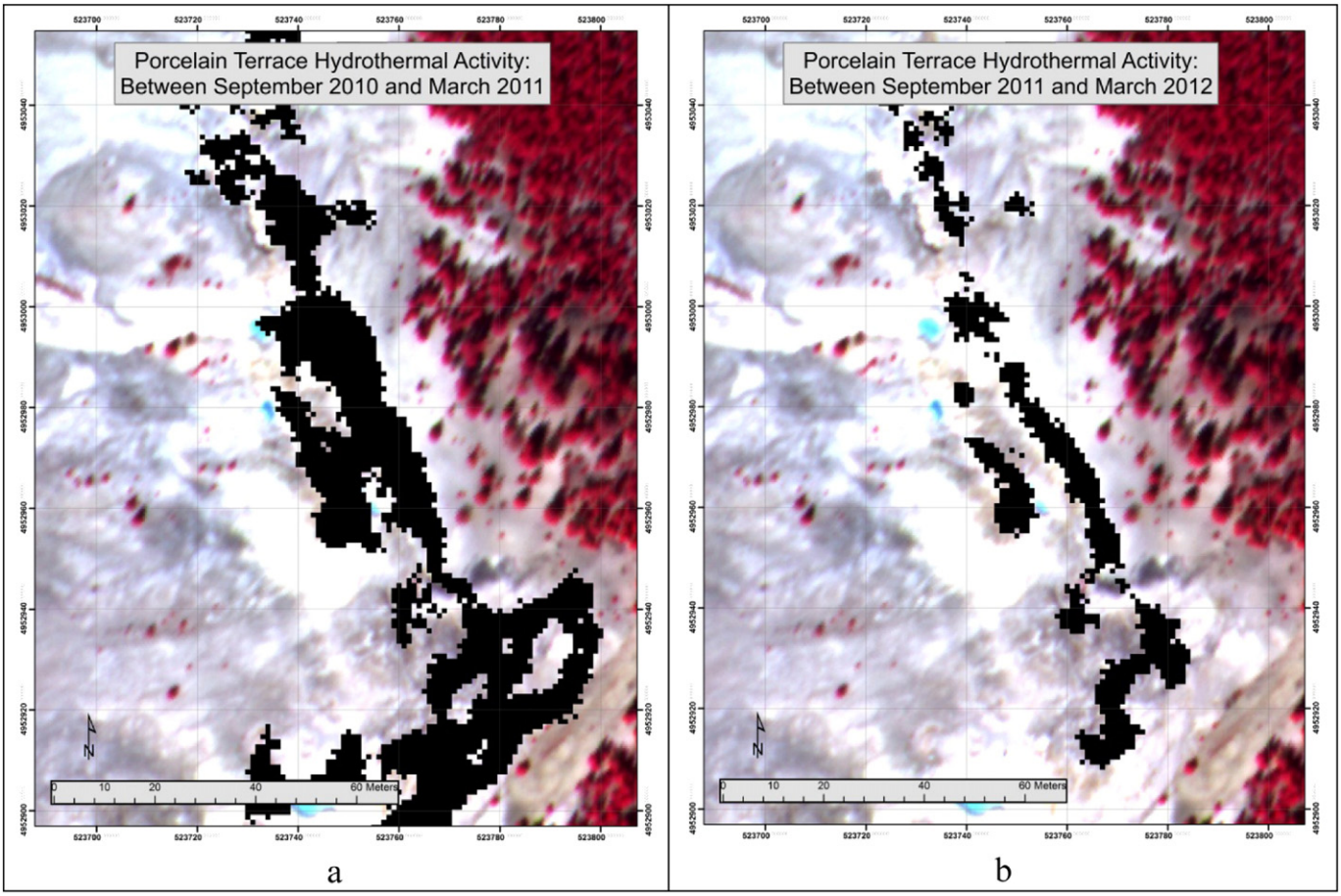

Fig. 13. a–b. Simple difference maps (black) for September 2010–September 2011 and September 2011–March 2012 draped over the 2010 false-color orthomosaic. Notice the NNW trending hydrothermal patterns from 2010 to 2012 and the 3–6 m offset between the 2010 visible orthomosaic (blue pool) and the black NNW trending difference maps for Porcelain Terrace. 2010 false-color orthomosaic available at www.mbmg.mtech.edu/gis/gis-ArcGISservices.asp, accessed 28 September 2015.

TIR acquisitions (2007–2008 and 2010–2012). Ground observations verified that the change detection technique at NGB identified changes in hydrothermal activity. For the entire night TIR mosaic, the NGB simple difference image for September 2010–September 2011 had a larger area of change (1,630,025 m^2) than the NGB simple difference image for September 2011–March 2012 (585, 815 m^2).

It is possible that the six-month difference between the September 2011 and March 2012 NGB images provided a useful time period for detecting change because less change had occurred over six months compared to over one year. Also, it may be useful to monitor hydrothermal changes between Fall and Spring acquisitions because there is minimal solar input both in Spring and Fall.

The high spatial resolution (1 m) of the night TIR imagery yielded valuable estimates of area with new or increased hydrothermal activity for HSB and NGB. For HSB, there were areas of changing hydrothermal activity in the Main Basin between 2007 and 2008 and changes in the Main Bain, East Basin and along Wrong Creek between 2010 and 2012. For NGB, the identified areas within Porcelain Basin and the Back Basin can be monitored using these techniques and the changing patterns of hydrothermal activity can be mapped over time. Future research will determine the applicability of these methods to other hydrothermal systems within Yellowstone National Park.

5. Conclusions

Airborne night TIR remote sensing with 1 m-spatial resolution has documented change within the HSB and NGB hydrothermal systems. The hydrothermal monitoring technique presented in this paper identified fracture-related hydrothermal changes between September 2010 and March 2012 for the NGB (Back Basin and Porcelain Terrace) and between September 2007 and March 2012 for HSB. These fracture-related changes at HSB and NGB may reflect local permeability changes in the hydrothermal system or changing permeability associated with ground deformation of the Yellowstone hydrothermal system. Field observations confirmed changes in hydrothermal activity in HSB and NGB. Even though the ambitious goal of 1 °C temperature accuracy was not met, the time-sequence of reproducible temperature patterns are valuable and a qualitative proxy for heat from these hydrothermal systems. Because residual solar heating is still present in the temperature maps for HSB and NGB, simple estimates of radiative heat flux using a background value to compensate for residual solar radiation would be premature.

Future research will concentrate on field experiments and gathering data to study the effects of solar heating and radiative cooling as a function of air temperature, wind speed and humidity and the variation at different times of the year. This research will involve the development of quantitative methods that may compensate for residual solar heating in the imagery and the presence of steam over hot pools, ultimately improving the precision of calculated, radiative surface temperatures from the airborne imagery.

Acknowledgements

The authors appreciate four reviewer's comments for substantially improving this paper. This research would not have been possible without the support of numerous individuals and institutions. The National

Park Service Rocky Mountain Cooperative Ecological Study Units Agreements (RM-CESU J1580050583, J1580050608, and J1580090425) provided funds for TIR research of HSB, NGB and other hydrothermal systems. The Remote Sensing Services Laboratory in the Dept. of Civil and Environmental Engineering at Utah State University and the Utah Agricultural Experiment Station (UTA00793 UTA01140) also provided support. The LASSI LIDAR and imaging system was developed with funds from the Utah Science Technology and Research initiative (USTAR) at Utah State University.

References

Bastiaansen, W. G. M., Menenti, M., Feddes, R. A., & Holtslag, A. A. M. (1998). A remote sensing surface energy balance algorithm for land (SEBAL): 1. Formulation. *Journal of Hydrology*, *212*, 198–212.

Berk, A., Bernstein, L. S., & Robertson, D. C. (1989). *MODTRAN: A moderate resolution model for LOWTRAN 7. Report GL-TR-89-0122*. Bedford, Maryland, USA: Geophysics Laboratory.

Brunsell, N. A., & Gillies, R. (2002). Incorporating surface emissivity into a thermal atmospheric correction. *Photogrammetric Engineering & Remote Sensing Journal (ASPRS)*, *68*(12), 1263–1269.

Cai, B., & Neale, C. M. U. (1999). A method for constructing 3-dimensional models from airborne imagery. *Color photography and videography for resource assessment. Proceedings of the 17th Biennial workshop*. Bethesda, MD: American Society for Photogrammetry and Remote Sensing.

Chang, W. L., Smith, R. B., Wicks, C., Farrell, J. M., & Puskas, C. M. (2007). Accelerated uplift and magmatic intrusion of the Yellowstone caldera, 2004 to 2006. *Science*, *318*(5852), 952–956.

Christiansen, R.,. L. (2001). The quaternary and pliocene Yellowstone plateau volcanic field of Wyoming, Idaho, and Montana. *U.S. geological survey professional paper 729-G* (145 pp.).

Dzurisin, D., Wicks, C. W., & Poland, M. P. (2012). History of surface displacements at the Yellowstone Caldera, Wyoming, from leveling surveys and InSAR Observations, 1923–2008. *U.S. geological survey professional paper 1788* (68 pp.).

Friedman, I. (2007). Monitoring changes in geothermal activity at Norris Geyser Basin by satellite telemetry, Yellowstone National Park, Wyoming. In M. L.A. (Ed.), *Integrated geoscience studies in the greater Yellowstone area. U.S. geological survey professional paper 1717* (pp. 513–532).

Geli, H. M. E., Neale, C. M. U., Watts, D., Osterberg, J., De Bruin, H. A. R., Kohsiek, W., ... Hipps, L. E. (2012). Scintillometer-based estimates of sensible heat flux using LIDAR-derived surface roughness. *Journal of Hydrometeorology*, *13*, 1317–1331.

Haselwimmer, C., Prakash, A., & Holdmann, G. (2013). Quantifying the heat flux and outflow rate of hot springs using airborne thermal imagery: Case study from pilgrim Hot Springs, Alaska. *Remote Sensing of Environment*, *136*, 37–46.

Huang, H. H., Lin, F. C., Schmandt, B., Farrell, J., Smith, R. B., & Tsai, V. C. (2015). The Yellowstone magmatic system from the mantle plume to the upper crust. *Science*, *348*(6236), 773–776.

Jackson, R. D., Clarke, T. R., & Moran, M. S. (1992). Bidirectional calibration results of 11 Spectralon and 16 BaSO4 reference reflectance panels. *Remote Sensing of Environment*, *40*, 231–239.

Jaworowski, C., Heasler, H. P., Hardy, C. C., & Queen, L. P. (2006). Control of hydrothermal fluids by natural fractures at Norris Geyser Basin. *Yellowstone Science*, *14*, 13–23.

Jaworowski, C., Heasler, H. P., Neale, C. M. U., Sivarajan, S., & Masih, A. (2013). Temporal and spatial variations of the Hot Spring Basin hydrothermal system, Yellowstone National Park, USA. *Remote Sensing*, *5*(12), 6587–6610.

Heasler, H. P., Bueter, L., & Jaworowski, C. (2011). Hydrothermal changes along the Norris Bask Basin Boardwalk. *Yellowstone National Park Geology program internal report* (11 pp.).

Kustas, W. P., & Norman, J. M. (1999). Evaluation of soil and vegetation heat flux predictions using a simple two-source model with radiometric temperatures for partial canopy cover. *Agricultural and Forest Meteorology*, *94*, 13–29.

Li, F., Kustas, W. P., Prueger, J. H., Neale, C. M. U., & Jackson, J. T. (2005). Utility of remote sensing based two-source energy balance model under low and high vegetation cover conditions. *Journal of Hydrometeorology*, *6*, 878–891.

Li, Z. L., Tang, B. H., Wu, H., Ren, H. Z., Yan, G. J., Wan, Z. M., ... Sobrino, J. A. (2013). Satellite-derived land surface temperature: Current status and perspectives. *Remote Sensing of Environment*, *131*, 14–37.

Neale, C. M. U., Pack, R. T., Sivarajan, S., & Masih, A. (2013). Visualization of the Mammoth hydrothermal system, Yellowstone National Park headquarters and the controlled groundwater area of the Montana compact. *Final report for CESU USURM-90 J1580100509 from 2010 to 2012* (13 pp.).

Neale, C. M. U., Geli, H. M. E., Kustas, W. P., Alfieri, J. G., Gowda, P. H., Evett, S. R., ... Howell, T. A. (2012). Soil water content estimation using a remote sensing based hybrid evapotranspiration modeling approach. *Advances in Water Resources*, *50*, 152–161.

Neale, C. M. U., & Crowther, B. (1994). An airborne multispectral video/radiometer remote sensing system: Development and calibration. *Remote Sensing of Environment*, *49*(3), 187–194.

Roberts, D. A., Quattrochi, D. A., Hulley, G. C., Hook, S. J., & Green, R. O. (2012). Synergies between VSWIR and TIR data for the urban environment: An evaluation of the potential for the hyperspectral infrared imager (HysplRI) decadal survey mission. *Remote Sensing of Environment*, *117*, 83–101.

Savage, S. L., Lawrence, R. L., Custer, S. G., Jewett, J. T., Powell, S. L., & Shaw, J. A. (2010). Review of alternate methods for Estimating Terrestrial Emittance and geothermal heat flux for Yellowstone National Park using landsat imagery. *GIScience & Remote Sensing*, *47*(4), 460–479.

Sundararaman, S., & Neale, C. M. U. (1997). Geometric calibration of the USU videography system. *Videography and color photography for resource assessment. Proceedings of the 16th Biennial workshop*. Bethesda, MD: American Society for Photogrammetry and Remote Sensing.

Taghvaeian, S., & Neale, C. M. U. (2011). Water balance of irrigated areas: a remote sensing approach. *Hydrological Processes*, *25*(26), 4132–4141.

Torgesen, C. E., Faux, R. N., Mcintosh, B. A., Poage, N. J., & Norton, D. J. (2001). Airborne thermal remote sensing for water temperature assessment in rivers and streams. *Remote Sensing of Environment*, *76*, 386–398.

Quatrtrochi, D. A., & Luvall, J. C. (2003). *Thermal remote sensing in land surface processes*. Boca Raton, Florida: CRC Press.

Watson, F. G. R., Lockwood, R. E., Newman, W. B., Anderson, T. N., & Garrott, R. A. (2008). Development and comparison of Landsat radiometric and snow-pack model inversion techniques for estimating geothermal heat flux. *Remote Sensing of Environment*, *112*(2), 471–481.

Vaughan, R. G., Kezthelyi, L. P., Lowenstern, J. B., Jaworowski, C., & Heasler, H. (2012). Use of ASTER and MODIS thermal infrared data to quantify heat flow and hydrothermal change at Yellowstone National Park. *Journal of Volcanology and Geothermal Research*, *233-234*, 72–89.

White, D. E., Hutchinson, R. A., & Keith, T. E. (1988). Geology and remarkable thermal activity of Norris Geyser Basin, Yellowstone National Park, Wyoming. *US Geological survey professional paper 1456* (75 pp).